



ELSEVIER

Ultramicroscopy 86 (2001) 303–318

ultramicroscopy

www.elsevier.nl/locate/ultramic

Valence electron energy loss study of Fe-doped SrTiO₃ and a Σ 13 boundary: electronic structure and dispersion forces

K. van Benthem^{a,*}, R.H. French^b, W. Sigle^a, C. Elsässer^a, M. Rühle^a

^a Max-Planck-Institut für Metallforschung, Seestraße 92, D-70174 Stuttgart, Germany

^b DuPont Corporation Central Research, E356-384, Exp. St., Wilmington DE 19880-0356, USA

Received 14 July 2000; received in revised form 11 September 2000

Abstract

Valence electron energy loss spectroscopy in a dedicated scanning transmission electron microscope has been used to obtain the interband transition strength of a Σ 13 tilt grain boundary in SrTiO₃. In a first step the electronic structure of bulk SrTiO₃ has been analysed quantitatively by comparing VEELS spectra with vacuum ultraviolet spectra and with *ab initio* density of states calculations. The electronic structure of a near Σ 13 grain boundary and the corresponding dispersion forces were then determined by spatially resolved VEELS. Also the effects of delocalization of the inelastic scattering processes were estimated and compared with results from the literature. © 2001 Elsevier Science B.V. All rights reserved.

PACS: 82.80.P; 61.72.M; 78.20

Keywords: Electron energy-loss spectroscopy; VEELS; SrTiO₃; Grain boundary; Electronic structure; Delocalization; Interband transitions; Optical properties

1. Introduction

Materials crystallizing in the perovskite structure are used in applications such as oxygen sensors, actuators, capacitors or simply as substrates for thin film growth. Since polycrystalline material is used frequently, the influence of grain boundaries (GBs) on the material properties may be essential. As an example it is well known that GBs can reduce the ionic conductivity (e.g. [1–6]),

especially in doped materials. This is often ascribed to the formation of space charge layers which compensate the charge of dopants or impurities segregated to the grain boundary thus leading to the formation of a double Schottky barrier (see e.g. [7]), whose space charge layer can have a spatial extent of several tens of nanometers. In addition, high-angle, or high Σ GB can exhibit substantial changes from the bulk material, with impurity and/or cation segregation or depletion at the boundary, changes in oxidation due to differences in the stoichiometry, and even changes in physical density because of linear or volumetric expansions of the material at the grain boundary. These types of phenomena are more often seen at

*Corresponding author. Tel.: +49-711-2095-311; fax: +49-711-2095-320.

E-mail address: benthem@hrem.mpi-stuttgart.mpg.de (K. van Benthem).

highly disordered, high Σ boundaries than at the lower energy, low Σ boundaries that have been typically the focus of research.

Ernst et al. [4] demonstrated that different GBs show significant differences in their physical and chemical properties. They showed that in SrTiO₃ doped with 0.14 wt% Fe some GB, like the $\Sigma 3$ or $\Sigma 5$ boundary are well structured and exhibit good oxygen ion transport, while the $\Sigma 13$ boundary has very reduced oxygen ion transport. They were able to correlate these findings with structural properties at the boundaries. In contrast to the $\Sigma 5$ and $\Sigma 3$ GBs the atomic structure of the $\Sigma 13$ boundary showed significant disorder in the boundary region, and from high-resolution transmission electron microscopy (HRTEM) images a width of this disordered grain boundary region of the order of 1 nm was discerned (Fig. 1). They also looked at compositional differences in the disordered material at the $\Sigma 13$ grain boundary and found a small enrichment of the Ti to Sr cation ratio at the boundary accompanied by Fe segregation (0.3 atoms nm⁻²) to the boundary. These studies did not address whether there was an absolute depletion of Sr or an absolute enrichment of Ti in the disordered material at the boundary. Also no comments were given by Ernst et al. [4] concerning a change in density for the disordered material relative to bulk SrTiO₃.

In the present work we measured the energy-loss which fast electrons suffer by collective electron

excitations (plasmons) or by single valence electron excitations into unoccupied states of the conduction band (valence electron energy-loss spectroscopy, VEELS). By using a dedicated scanning transmission electron microscope (STEM) the spatial resolution of this technique is mainly limited by the probe size of the electron beam, the delocalization of the inelastic scattering process [8,9] and by the specimen thickness [10,11]. In the low-loss region studied here, the contribution of delocalization is predicted to vary with energy and can be important up to an energy loss of ~ 30 eV. Pennycook et al. [8] predict an energy dependence of the delocalization of 6 nm at $\Delta E = 5$ eV to 1 nm at $\Delta E = 30$ eV. Notwithstanding this limitation, grain boundary specific VEELS spectra may be obtained by scanning the electron beam across the grain boundary. VEEL spectroscopy has been successfully applied to a number of material systems [12–17] in order to determine the full complex dielectric function from which all optical properties can be obtained.

Because of the important role of GBs in SrTiO₃ and the presence of a disordered layer at the $\Sigma 13$ boundary, the question arises whether the $\Sigma 13$ boundary can be considered as an interface with a disordered intergranular material. In such cases long-range London dispersion (LD) forces arise due to changes in electronic structure and optical properties at the interface relative to the bulk [18,19]. We therefore calculate the Hamaker constants of the London dispersion forces at the $\Sigma 13$ boundary directly from the spatially resolved VEELS data. For the case of silicate intergranular films seen in silicon nitride ceramics a correlation exists between van der Waals forces and the thickness of the intergranular film [18,20,21]. The magnitude of the attractive London dispersion force between two grains that arise at a grain boundary is expected to be very low for a dense, atomically abrupt interface, while for a boundary such as the $\Sigma 13$ boundary, in which a nanometer scale layer of disordered intergranular material is present, the London dispersion force may be appreciable and play a role in the boundary thickness, the thermodynamic driving forces for segregation or depletion at the boundary, and the adhesion or strength of the interface.

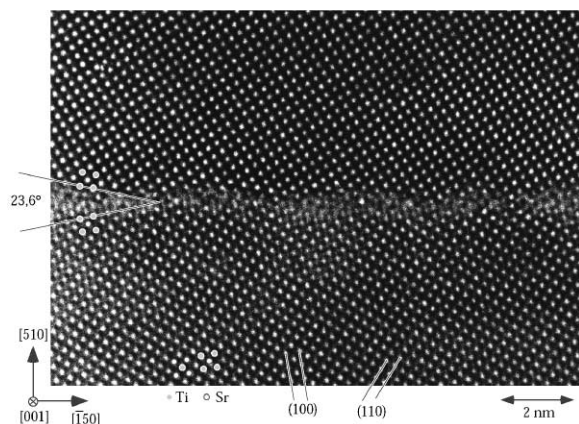


Fig. 1. HRTEM image of the $\Sigma 13$ grain boundary in SrTiO₃ in [00 1] zone-axis orientation [21].

2. Methods

2.1. Electron microscopy

2.1.1. Sample preparation

Tilt GBs with a near $\Sigma 13$ (510) $\theta = 24^\circ$ orientation relationship were prepared by diffusion bonding (Wako-Bussan Ltd. and Shinkosha Ltd. Tokyo, Japan). As starting material Fe (0.14 wt%)-doped SrTiO₃ single crystals were used which were grown by the Verneuil method [22]. Cross-sectional TEM specimens were prepared by the method described by Strecker et al. [23]. Ion beam thinning was performed using a Gatan DUOMILL600 (12°, 6 keV). After perforation the specimen was further ion-milled at 3 keV in order to remove most of the damage of the specimen surfaces. In order to decrease contamination effects the specimens were plasma-cleaned prior to insertion into the microscope and baked inside the airlock for 20 min. This procedure considerably reduced the growth of carbon contamination layers on electron-irradiated areas. As shown later, such layers lead to artificial structures in the VEELS spectra superimposed on the SrTiO₃ signal (cf. Fig. 4). The specimen thickness ranged from 2.0 to 2.5 multiples the inelastic mean free path λ to minimize influences of surface plasmons and effects by contamination or beam damage due to specimen preparation.

2.1.2. Data acquisition

The VEELS-measurements were performed with a Gatan PEELS766 parallel electron energy-loss spectrometer attached to a VG HB501 UX dedicated scanning transmission electron microscope (STEM) operating at 100 keV. The beam current was reduced to less than 1 nA in order to improve the energy resolution to 0.6 eV (FWHM of zero-loss peak). The electron probe size was below 1 nm. Spectra were acquired using a dispersion of 0.1 eV/channel in order to record spectra up to an energy loss of 90 eV. The convergence semiangle was chosen equal to the collection semiangle, which was given by the 2 mm PEELS aperture to 6.5 mrad. In the low-loss regime this leads to an underestimation of the measured EELS intensities by about 10% [11]. A

correction for these effects, e.g. by using the CONCOR program [11], would lead to only small changes in intensity of the interband transition strength. Since all spectra were analyzed consistently no substantial changes are expected in the final results. One hundred single spectra were acquired while scanning the probe perpendicularly across the interface with scanlengths between 20 and 100 nm. In case of specimen drift a cross-correlational spatial drift correction was performed after every 5 spectra during acquisition. All spectra were corrected for dark current of the photodiode array. Influences of detector gain variations on the analysed data could not be observed. Data acquisition with the PEELS detector was performed with the Gatan Digital Micrograph 3.3 Spectrum Imaging software using a Macintosh PowerPC. Since the dynamic range of the detector is 16 bits, the zero-loss peak and the plasmon-loss peaks were not recorded in the multiplexed manner as in previous VEELS studies [13,14,17,18]. This prevents errors which might occur by fitting the zero-loss peak to the energy-loss region.

2.1.3. Data analysis

For all VEEL spectra the center of the zero-loss peak was fitted for the zero energy calibration. Subsequently, the spectra were corrected for multiple scattering events by Fourier-log deconvolution [11]. During this procedure the wings of the zero-loss peak were fitted separately with an asymmetric PearsonVII line shape [13]. This fitting was performed up to 50% of the height of the zero-loss peak. For energies lower than 3.4 eV, i.e. close to the band gap energy of SrTiO₃ (3.2 eV [24], 3.1 eV [25–27]), no transitions are expected and therefore the intensity of the SSD spectrum below this value is set to zero [15] (cf. Fig. 2). Unlike in optical spectroscopy, in energy-loss spectroscopy extra intensities due to Cerenkov radiation can occur in the low-energy region below 10–15 eV. Such effects were not considered in this work since the VEEL spectra show the same line shape as the VUV spectra in this energy regime. Influences of a variation of the cut-off energies within ± 0.3 eV could be neglected. The resulting energy-loss function (ELF) is proportional to $\text{Im}(-1/\epsilon)$ [11],

where $\varepsilon = \varepsilon_1 + i\varepsilon_2$ is the complex dielectric function. To obtain the real part of the dielectric function $\text{Re}(-1/\varepsilon)$ a FFT-based Kramers–Kronig analysis [21,28–30] was applied. Therefore, the spectra were extrapolated to 1000 eV on the high-energy side. From the dielectric function the interband transition strength J_{cv} is calculated following

$$J_{cv} = J_{cv1} + iJ_{cv2} = \frac{m_0^2}{e^2 \hbar^2} \frac{E^2}{8\pi^2} i(\varepsilon_2(E) + i\varepsilon_1(E)), \quad (1)$$

where m_0 is the electron mass, e its charge and E the energy-loss. For a correct scaling of J_{cv} the index sum rule with the refractive index $n = 2.37$ for Fe-doped SrTiO₃ was used as determined by spectroscopic ellipsometry [31,32]. In the literature, values for the refractive index between 2.20 and 2.66 are reported due to changes in the composition, stoichiometry, and strain of the SrTiO₃ specimens [15]. J_{cv1} and J_{cv2} correspond to the joint density of states and are proportional to $E^2 \varepsilon^*$, where ε^* denotes the complex conjugate of ε . The analysis of the spectra was done with Electronic Structure Tools [33] consisting of VEELS analysis, Kramers–Kronig analysis and Hamaker constant calculation.

The effective number of electrons n_{eff} contributing to transitions up to energy E can be calculated using the oscillator strength or f sum rule [11,34] shown in Eq. (2), evaluated on J_{cv1} :

$$n_{\text{eff}}(E)|_{J_{cv1}} = \frac{4v_f}{m_0} \int_0^E \frac{J_{cv1}(E')}{E'} dE', \quad (2)$$

where v_f is a characteristic volume of material corresponding to either one chemical formula unit or in the present work, a cubic centimeter volume.

2.2. Vacuum ultraviolet spectroscopy

VUV spectroscopy was performed on a diamond-polished Fe (0.14 wt%) -doped SrTiO₃ single-crystal sample so as to determine the VUV reflectivity and by Kramers–Kronig analysis the interband transition strength of the bulk material. These results will be discussed in greater detail elsewhere [35].

VUV spectroscopy has become an established technique for electronic structure studies of large band-gap, insulating ceramics. The VUV spectrophotometer, the details of which have been discussed previously [31], utilizes a laser plasma light source (LPLS) [32] and iridium reference mirrors. The energy range of the instrument is from 1.7 to 44 eV, or from wavelengths of 700 nm to 28 nm which extends beyond the air cutoff of 6 eV and the window cutoff of 10 eV. The resolution of the instrument is 0.2–0.6 nm which corresponds to 16 meV resolution at 10 eV and 200 meV resolution at 35 eV.

Spectroscopic ellipsometry was performed with the Woollam 193/DUV instrument, which has a range from 1.13 to 6.67 eV (1100–186 nm), and employs MgF₂ polarizers and analyzers rather than the more common calcite optics. The instrument measures the ellipsometric parameters ψ and Δ , defined by the equation

$$\tan(\psi)e^{i\Delta} = \frac{R_p}{R_s}, \quad (3)$$

where R_p/R_s is the complex ratio of the p- and s-polarized components of the reflected amplitudes. These parameters are analyzed using the Fresnel equations [36] in a computer-based modeling technique to directly determine the thin film's optical constants.

2.3. Band structure calculation

Self-consistent ab initio band-structure calculations based on the density functional theory (DFT) [37,38] were performed in the local density approximation (LDA) [39,40] using norm-conserving pseudopotentials and a mixed basis of localized wave functions and plane waves [41–44]. We used the cubic unit cell of the perovskite structure, containing one strontium, one titanium, and three oxygen atoms. The site projected density of states (PDOS) were obtained from the Kohn–Sham energy eigenstates on a mesh of $8 \times 8 \times 8$ k-points in the first Brillouin zone by projection onto partial waves in spheres at the atomic sites Sr, Ti, and O. The energy E_F (Fermi energy) of the highest occupied one-electron state at the valence band edge is taken as the energy zero. Projection

radii were chosen as 2.607 bohr (1 bohr = 0.529 Å) for Sr, 1.525 bohr for Ti, and 2.840 bohr for O. With these radii, the atomic spheres contain the formal charges, i.e. +2 for Sr, +4 for Ti, and –2 for O, respectively. A Gaussian broadening of the PDOS of 0.5 eV full-width at half-maximum was applied. The calculational results (Fig. 8) will be discussed in detail in Section 4.1.

2.4. Hamaker constant calculations

Once the electronic structure of bulk Fe-doped SrTiO₃ and of the intergranular material present at the Σ13 boundary have been determined, then the full spectral Hamaker constant [20] can be determined using the Lifshitz method. These have been covered in detail elsewhere [19], and are only summarized here. For the case of two grains of material 1 which are separated from each other by an intervening intergranular material, material 2, the Hamaker constant, A_{121}^{NR} , determines the magnitude of the van der Waals force between the two grains. The intergranular material serves to shield the attraction of the two materials. The Hamaker constant is large for a vacuum interlayer, and is zero if the interlayer material 2 is identical to the grain's material 1:

$$A_{121}^{\text{NR}} = -6\pi L^3 F_{\text{vdW}}. \quad (4)$$

To calculate the London dispersion force, the major component of the van der Waals forces, we utilize another Kramers–Kronig dispersion relation to produce the London dispersion spectrum, $\varepsilon_2(\xi)$, which is an integral transform of the imaginary part of the dielectric constant from a function of the real frequency ω to a function of the imaginary frequency ξ . The London dispersion spectrum is a material's property and represents the retardation of the oscillators:

$$\varepsilon_2(\xi) = 1 + \frac{2}{\pi} \int_0^\infty \frac{\omega \varepsilon_2(\omega)}{\omega^2 + \xi^2} d\omega. \quad (5)$$

Once the London dispersion spectra of the two materials are determined, the Hamaker constant is calculated using integrals of spectral differences, which are discussed in more detail in [19].

3. Results

3.1. Bulk

As we are working with quantitative optical properties for both the energy-loss function and J_{cv} , changes in amplitude are not related to changes in specimen thickness. The effects of thickness are accounted for in the single-scattering deconvolution to remove multiple-scattering effects, and the amplitude of the energy-loss function is determined by the index sum rule for the bulk material. Therefore, changes in the amplitude of the ELF or J_{cv} are directly related to changes in the electronic structure of the material.

Fig. 2 shows the energy loss function (ELF) and Fig. 3 shows the interband transition strength J_{cv} of bulk SrTiO₃ which was obtained by VUV spectroscopy and by VEELS. One can clearly identify peaks labeled a–h in the ELF spectra and A'–H in the J_{cv} spectra. The exact energetic positions of these peaks are given in Tables 1 and 2. Additional peaks occurring in the VUV spectra which are not visible in VEELS because of differences in the experimental energy resolution are not included in Table 2. The interband transitions (Figs. 3 and 7) are dominated by excitations around 5.5 eV (doublet A' and A), by a triplet around 12 eV (peaks B, C, and D) and by excitations of 27.3 eV (F) and 45.5 eV (H). Weaker features occur at 16.5 eV (E'), 20.1 eV (E), 26.1 eV as a small extra peak (F') and at 37.5 eV (G). Apart from that, small spectral features can be observed between peaks E and F' which cannot be analysed in detail because they are superimposed by the broad peak labeled F. The peak energies in the J_{cv} spectra obtained by VEELS and VUV spectroscopy are the same within uncertainties of ± 0.2 eV and reproduce results from previous VUV spectroscopy investigations [45]. A detailed comparison of VUV and VEEL spectroscopy of bulk SrTiO₃ and Fe-doped SrTiO₃ will be given elsewhere [35] and is not part of this work. The density of states (DOS) for SrTiO₃ is presented in Fig. 8 along with the orbital decomposition of the DOS into Sr, Ti, and O partial DOS. The energy dependence of the projected densities of states (PDOS) and their atomic origins

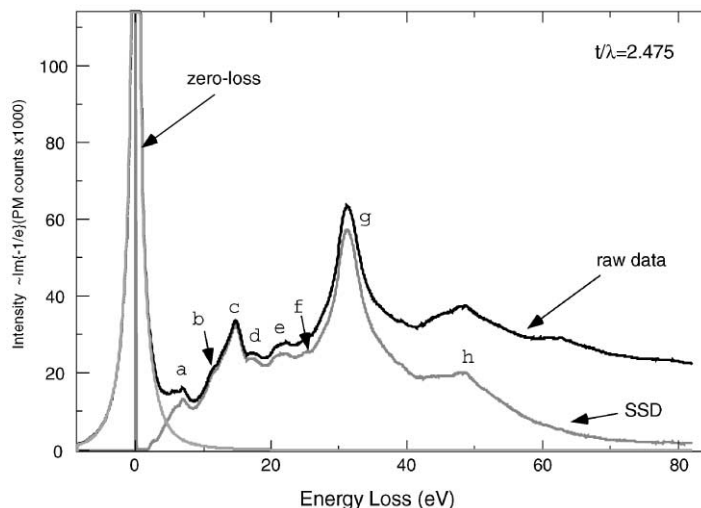


Fig. 2. Valence EEL spectrum of bulk SrTiO₃, the extracted zero-loss peak (green) and the corresponding single-scattering spectrum after Fourier-log deconvolution (SSD). The specimen thickness was $t/\lambda = 2.475$.

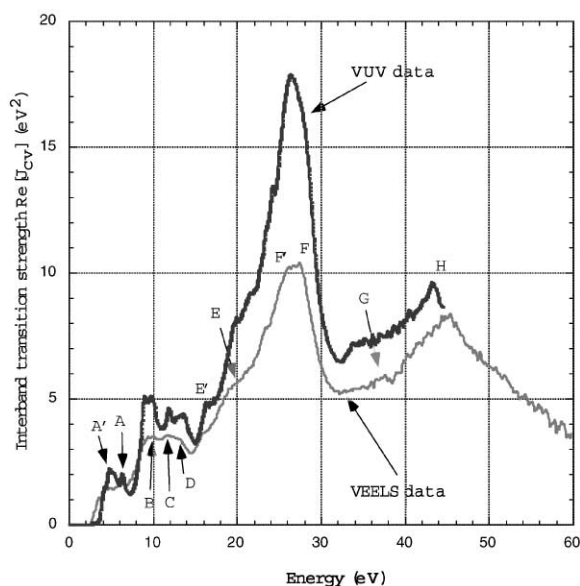


Fig. 3. Interband transition strength ($\text{Re}[J_{cv}]$) of bulk SrTiO₃ obtained by VEEL and by vacuum ultraviolet (VUV) spectroscopy.

will be very useful in the assignment of the interband transitions seen in the interband transition strengths in the next section.

After keeping the electron beam on a specimen area for an extended period of time, an extra

Table 1

Peak positions (in eV) of the energy loss function of bulk SrTiO₃ as labeled in Fig. 2

	a	b	c	d	e	f	g	h
Pure bulk	7.0 ^a	11.9	14.8	17.2	22.3	25.0	31.3	47.8

^a Peak a seems to be split into two parts in the bulk spectrum, which could not be resolved in these spectra.

broad peak in the energy-loss function occurred at about 25 eV energy loss. The peak height increased with irradiation time (see Fig. 4). This was also observed by Ryen et al. [15] and was assigned to energy-losses due to plasmon excitations within a contamination layer forming during electron irradiation. Due to this effect integration times were chosen such that this artificial peak did not occur. However, beam damage effects by ion-beam thinning at the specimen surface [46] can be responsible for an overall loss of intensity in the SSD spectra.

3.2. $\Sigma 13$ boundary

Fig. 5 shows the energy-loss functions at 100 spots of a linescan with a scan length of 40 nm

Table 2

Interband transition energies (in eV) in bulk SrTiO₃ in comparison to our LDFT calculations of the density of states and to those of [45,51] as well as to VUV reflectivity experiments by Bäuerle et al. [45]

	A'	A	B	C	D	E'	E	F'	F	G	H
VEELS (this work)	5.0	6.4	9.7	11.7	13.3	16.5	20.1	26.1	27.3	37.5	45.5
VUV (this work)	4.9	6.4	9.8	11.9	13.4	16.4	20.0	26.4	27.4		
VUV [45]	4.86	6.52	9.9	12.0	13.0	16.4	19.6	–	–	–	–
Theory (this work)	5.1	6.7–6.8	9.7	11.5–12.1	13.1	16.7	19.7–20.3	*	*	*	*
Theory [45,51]	5.0 [49]	6.5	8.5 [49]	11.7 [50]	13.3 [50]			*	*	*	*
Assignments	O 2p–Ti 3d t _{2g}	O 2p–Ti 3d t _{2g}	O 2p–Ti 3d e _g	O 2p–Ti 3d e _g O2p–Sr4d	O 2p–Sr 4d	Sr 4p–Ti 3d t _{2g}	Sr 4p–Ti 3d e _g	?	?	?	?

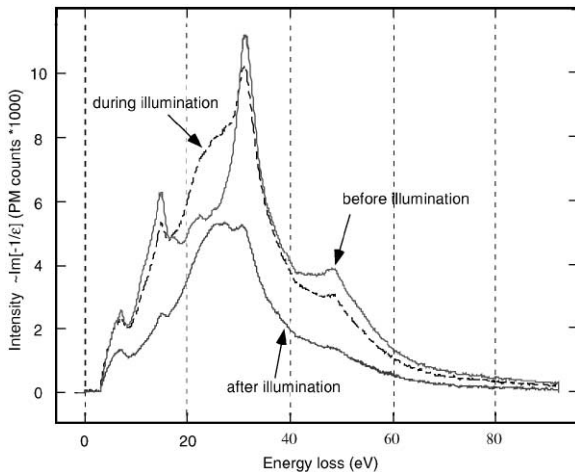


Fig. 4. Energy-loss functions before, during and after continuous electron illumination of bulk SrTiO₃.

which corresponds to 0.4 nm separation of subsequent spots. The magnitude of the energy loss function is color-coded. The position of the Σ 13 grain boundary is near the 20 nm distance tick and is marked by an arrow. By this top view of the data one can clearly identify the grain boundary, appearing as a dip in the data surface. Spectra well apart from the grain boundary (i.e. distances > 3 nm) show the same line shape for the

front grain and the back grain. Single features of the bulk spectra are shifted in energy or are completely absent at the grain boundary. Fig. 6 shows the same three-dimensional plot for the calculated real part of the interband transition strength $\text{Re}[J_{cv}]$. The Σ 13 boundary can again be identified by a dip in the data surface. In Fig. 7 two spectra out of this linescan, one directly from the GB and one from the grains are extracted and are plotted versus energy. The J_{cv} spectra of the two grains were found to be identical. The peak positions of the spectra are listed in Table 3. In the low-energy region below 8 eV no significant features, except for a small remnant of A'–A remain evident in the boundary. The triplet structure B–C–D observed in bulk SrTiO₃ disappears. At 13.6 eV a new peak labeled D* occurs at the grain boundary. This can be a new grain boundary specific feature or just the bulk peak D shifted by 0.3 eV towards higher energies. The transitions E and E' at 20.1 and 16.5 eV, respectively, are reduced in intensity but remain. The most intense transition labeled F at 27.3 eV shifts by 1.1 eV to higher energies whereas the slight shoulder F' at 26.1 eV disappears at the grain boundary. The weak feature labeled G at 37.5 eV as well as the strong peak at 45.5 eV labeled H remain constant in their energy position at the grain boundary.

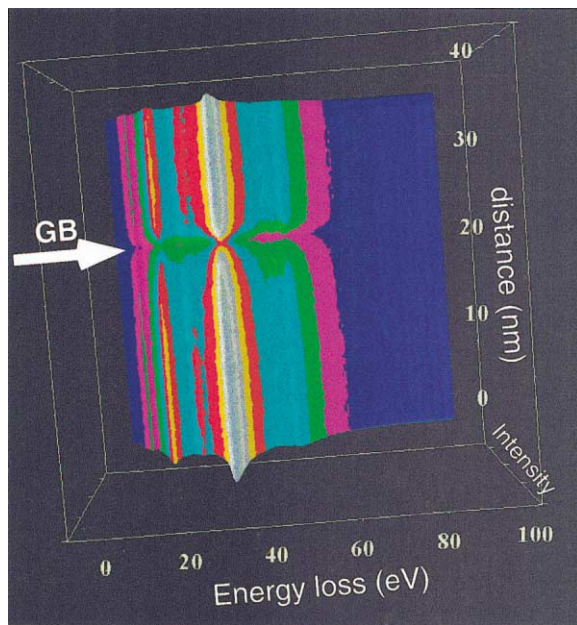


Fig. 5. Linescan of the energy loss function (ELF) across the $\Sigma 13$ grain boundary (GB) after single-scattering deconvolution.

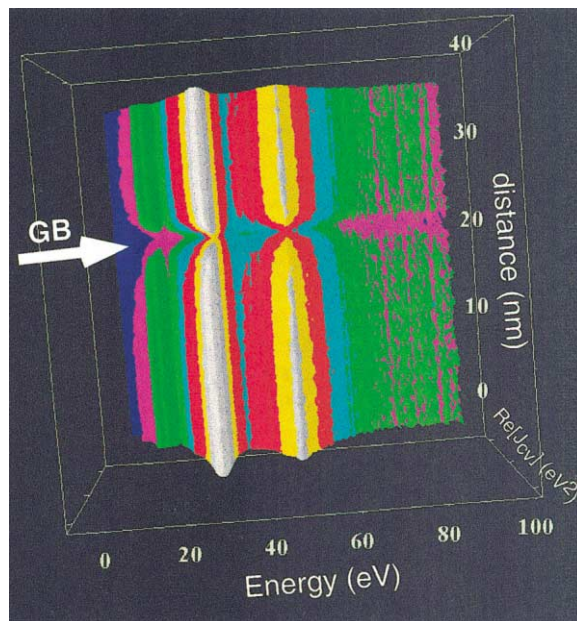


Fig. 6. Linescan of the real part of the interband transition strength ($\text{Re}[J_{cv}]$) across the $\Sigma 13$ grain boundary (GB).

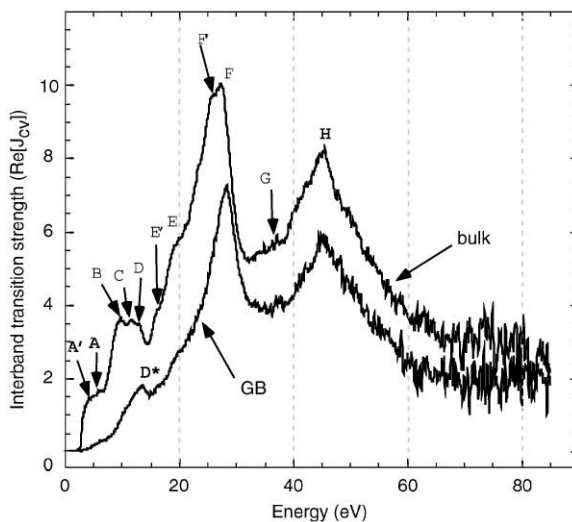


Fig. 7. Interband transition strength ($\text{Re}[J_{cv}]$) of bulk SrTiO_3 (bulk) and of the $\Sigma 13$ grain boundary (GB).

4. Discussion

In this section we will first analyze and discuss the results for the measurements of bulk SrTiO_3 , comparing the VEELS and VUV results with the DOS from the band structure calculation. This comparison will allow us to develop assignments for the transitions seen in the interband transition strength. Based on this the electronic structure at the $\Sigma 13$ grain boundary will be analyzed in Section 4.2. Changes in the J_{cv} spectra across the grain boundary allow an analysis of the delocalization of the inelastic scattering process in the investigated energy regime. Finally, the dispersion forces for the investigated grain boundary with its segregated intergranular material are calculated.

4.1. Bulk electronic structure from VEELS

Since the real part of J_{cv} corresponds to transitions from occupied valence band states to unoccupied conduction band states, assignments of the orbital origins of these transitions can be obtained by a comparison with DOS calculations near the Fermi level. Such calculations on SrTiO_3 have been performed by several authors [47–51].

Table 3

Peak positions (in eV) in the interband transition strength $\text{Re}[J_{\text{cv}}]$ for bulk SrTiO_3 and for the $\Sigma 13$ grain boundary

	A'	A	B	C	D	D*	E'	E	F'	F	G	H
Bulk	5.0	6.4	9.7	11.7	13.3	–	16.5	20.1	26.1	27.3	37.5	45.5
$\Sigma 13$	–	–	–	–	–	13.6	16.5	20.2	–	28.4	37.5	45.5

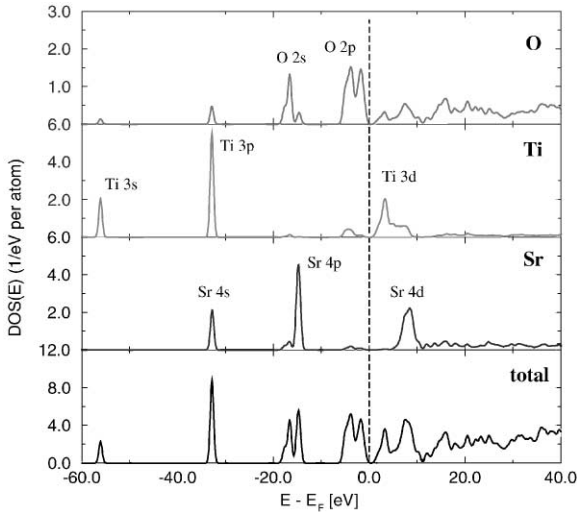


Fig. 8. Calculated total projected density of states (PDOS) for SrTiO_3 and the site projected PDOS for oxygen, titanium and strontium, respectively.

Fig. 8 shows our results of the PDOS calculations for pure SrTiO_3 projected onto the sites of Sr, Ti, and O. The most remarkable features are the deep valence states of Ti 3s (–56 eV) and 3p (–33 eV) and Sr 4s (–33 eV) and 4p (–14.7 eV) as well as the Ti 3d t_{2g} bands (+1.0 to +4.5 eV) and the Ti 3d e_g bands (+4.5 to +9.0 eV) and Sr 4d (+5 to +12 eV) states in the conduction band. The lowest energy interband transitions, occurring near the band gap energy of 3.2 eV [25–27], correspond to transitions from the O 2p upper valence band to the Ti 3d t_{2g} and e_g conduction bands.

By comparing possible interband transition energies from the DOS with the peak positions shown in Table 2 we can develop a model of the interband transition assignments. For a quantitative comparison of the band-structure calculations with the experimentally determined interband transition strength the transition matrix elements

would have to be calculated which has not been done in this work. Hence, in Table 2, the experimental peak positions are assigned to peak positions in the calculated DOS which are close in energy. The symmetry characters of the corresponding calculated states are used to assign the initial and final states of the transition (last line of Table 2; e_g and t_{2g} mark the splitting of the d states in the cubic crystal). Note that further transitions can be extracted from the calculated DOS than those visible in the experimental spectra (cf. Figs. 3 and 8) and listed in Table 2.

Transition A' and A originate from transitions of O 2p electrons into the Ti 3d t_{2g} band, while B and C correspond to O 2p to Ti 3d e_g transitions. Transition D is due to O 2p to Sr 4d excitations. Peak D also has contributions from O 2p \rightarrow Sr 4d transitions since the Sr 4d DOS becomes large at energies between 5 and 12 eV (cf. Fig. 8). At transition energies of 16.5 eV (E') and 20.1 eV (E) the interband transition strength shows two shoulders (Fig. 7) which are due to Sr 4p \rightarrow Ti 3d t_{2g} and e_g transitions, respectively. A spin-orbit splitting of the Sr 4p level by 0.6 eV [45], i.e. splittings within E' and E, are not observed in our VEELS and VUV measurements due to the experimental energy resolution. For final states with energies higher than about 15 eV above the Fermi energy the DOS shows a wealth of different overlapping energy levels resulting in broad and strongly structured energy bands (cf. Fig. 8). The quantitative description by computational electronic structure methods is getting increasingly difficult because of limitations in the number of k points, the completeness of basis sets, types of projection (spheres versus atomic orbitals) etc. Therefore an assignment of calculated states to measured peaks F', F, G, and H becomes ambiguous and questionable. However, as the O 2p energy levels and the Sr4p level are separated by

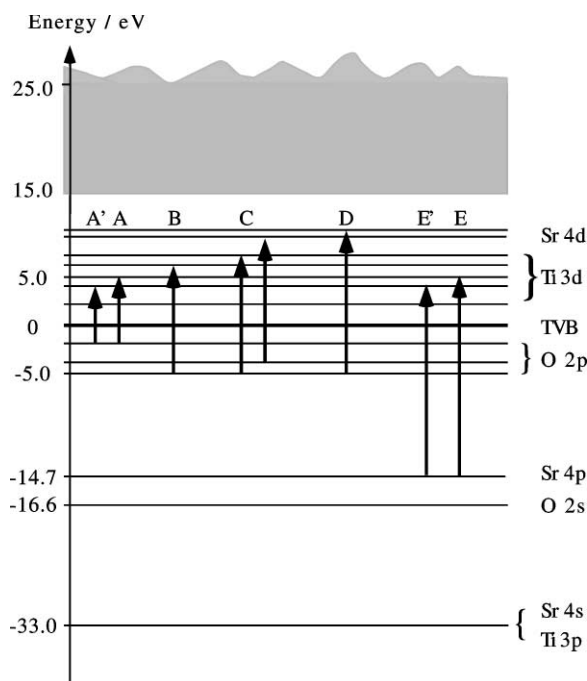


Fig. 9. Simplified energy level diagram for bulk SrTiO_3 . The transitions from the valence band into the conduction band assigned in this work are plotted in accordance to Table 2. Energies were taken from DOS calculations and are calibrated with respect to the top of the valence band (TVB).

10–13 eV and the transition energies of A' and E' differ by 11.5 eV, then Sr 4p to Ti 3d transitions should be observable on the left wing of feature F. For this reason, it is possible that the weak transitions below peak F have final Ti 3d t_{2g} and e_g states and origin from Sr 4p levels.

The described transitions given in Table 2 are plotted in a simplified energy level diagram for bulk SrTiO_3 in Fig. 9. Bäuerle et al. [45] have also proposed a schematic energy level diagram for SrTiO_3 based on a high level of agreement between their VUV reflectivity measurements and theoretical band structure calculations by Mattheiss [47]. They only assigned transitions from O 2p and Sr 4p into Ti 3d levels. The transitions A' to E found in this work are also found by Bäuerle and co-workers [45] within an energetic tolerance of ± 0.3 eV (cf. Table 2). As shown in Table 2 our assignments for the interband transitions are in good agreement with those of Bäuerle et al. [45].

Dipole-forbidden transitions could not be resolved in this work, although they were possible since a collection aperture of 6.5 mrad was used. No dipole-forbidden transitions would occur if collection apertures smaller than 3 mrad were used, as was calculated with the SIGPAR2 program by Egerton [11].

4.2. Electronic structure of the Σ_{13} boundary

Previous investigations on the Σ_{13} grain boundary have shown a disordered grain boundary structure of 0.6–0.9 nm width by HRTEM experiments [22,52]. Fe segregation to the intergranular film of 0.3 ± 0.05 atoms/nm² as well as a slight enrichment of titanium in comparison to strontium was observed by energy-dispersive X-ray measurements. Furthermore, a similar increase of the Ti/Sr ratio was found in very thin areas of the specimen, which can be due to a deficiency of Sr close to the surfaces which is known from ion thinning experiments [46]. Browning and co-workers [53] have found partially filled Ti/O and Sr/O columns in the grain boundary plane for high Σ symmetric and asymmetric [001] tilt GBs in pure SrTiO_3 .

The experimental VEELS data and the interband transition strength spectra show well-resolved differences at the grain boundary as compared to the bulk. The changes in the interband transition strength between the grains and the intergranular material at the Σ_{13} boundary arise due to changes in the electronic structure of the material. The assignment of transitions in the DOS to the peaks seen in the interband transition strength therefore allow us to understand these changes in the electronic structure and bonding of the Σ_{13} grain boundary.

At the grain boundary the overall intensity of the interband transition strength is reduced in comparison to the two grains. Fig. 10 shows the relative thickness t/λ , the index of refraction n , and the oscillator strength sum rule across the grain boundary. The relative thickness of the specimen nearly remains constant over the whole scanlength, with the slight taper of the sample evident. The index of refraction drops from 2.3 to 1.29 in the grain boundary region. This

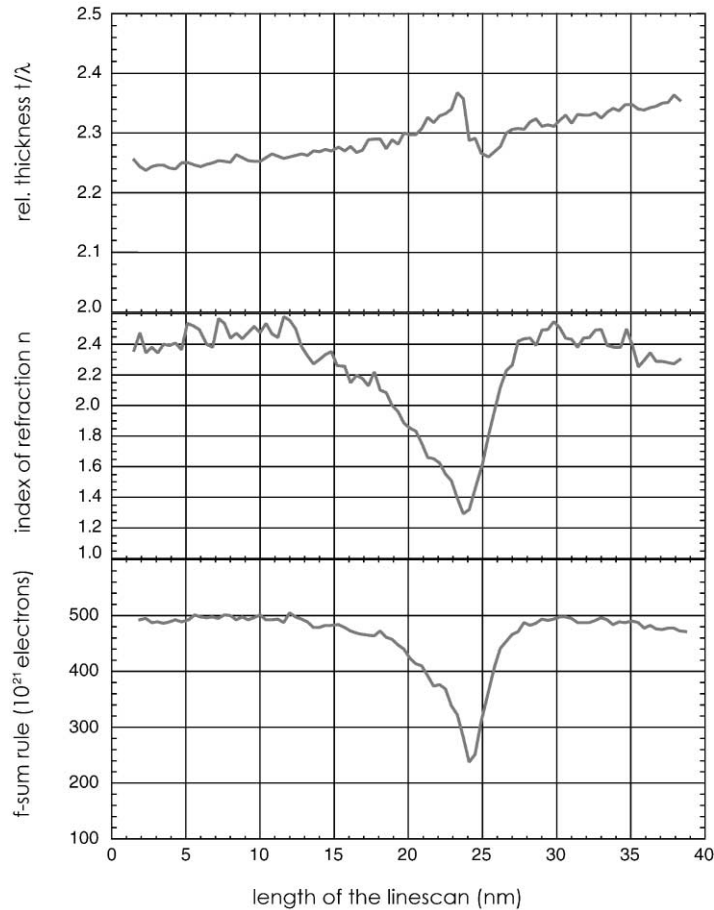


Fig. 10. Linescan of the relative specimen thickness t/λ , the index of refraction, and the oscillator strength sum rule across the $\Sigma 13$ grain boundary.

corresponds to lower density of the intergranular material compared to the bulk SrTiO_3 grains which explains the overall reduction of the interband transition strength in the grain boundary region. This reduction in density at the boundary is further confirmed by the corresponding dramatic reduction in the valence electron count, evaluated up to 90 eV, from $500 \times 10^{21} \text{ e}^-/\text{cm}^3$ in the SrTiO_3 grains down to $240 \times 10^{21} \text{ e}^-/\text{cm}^3$ in the $\Sigma 13$ boundary.

The reduction in intensity of peaks labeled A', B, C, and D can be interpreted as a loss of oxygen and/or a loss of titanium at the grain boundary.

Because of previous energy-dispersive X-ray measurements [22,52] which have shown an enrichment of Ti at the $\Sigma 13$ grain boundary, this loss of intensity is due to formation of oxygen vacancies in the grain boundary region. Therefore, the spectral feature labeled D* is caused by the formation of a grain boundary electronic transition and cannot be discussed as a slight enlargement of the O 2p \rightarrow Sr 4d transition energy, which would also be energetically possible.

Also spatially resolved electron energy-loss near-edge structure (ELNES) investigations, using the spatial difference method [54], of the

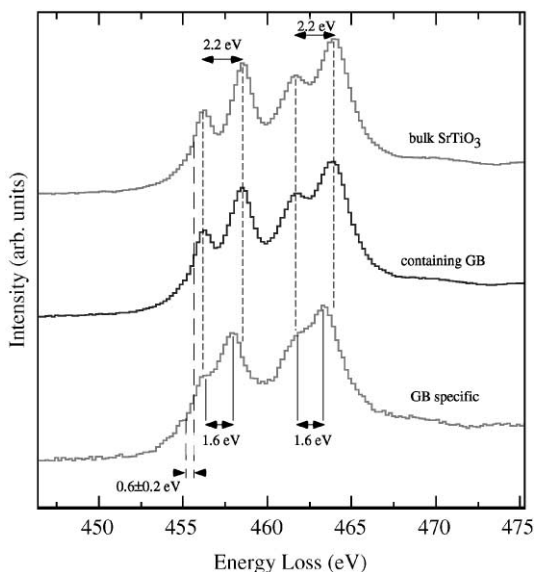


Fig. 11. Spatially resolved ELNES measurements of the Ti $L_{2,3}$ -edge of bulk SrTiO_3 , of a region containing the grain boundary (GB) and the extracted spatial difference spectrum [53] which represents the grain boundary specific ELNES component. The spectra were dark current and detector gain corrected and afterwards background subtracted using a power-law [11]. The collection semi-angle was 6.5 mrad. The specimen thickness was $t/\lambda = 0.55$.

Ti $L_{2,3}$ -edge were performed where a reduction of the crystal field splitting by 0.6 eV in the grain boundary region compared to the bulk material (cf. Fig. 11) was observed. A chemical shift of the Ti $L_{2,3}$ -edge by 0.6 ± 0.2 eV towards lower energy-losses was observed which indicates a reduced nominal oxidation state for Ti [55], i.e. a more metallic character in the grain boundary region. This also underlines the formation of oxygen vacancies at the grain boundary [55].

The observed reduction in density in the intergranular material and the formation of oxygen vacancies lead to a reduced splitting of the Ti t_{2g} and Ti e_g levels. Since core levels are relatively unaffected by density-related changes of bandwidths (e.g. Sr 4p levels) transition energies E' and E remain constant at the grain boundary. Band narrowing effects of the Ti t_{2g} and Ti e_g levels could not be resolved for these transitions. Although the origin of peaks F' and F could not be determined, peak F shifts significantly by 1.1 eV to

higher energy-losses in the grain boundary region. Finally, it can be concluded that the disordered intergranular film dramatically changes the electronic structure and therefore the optical and electrical properties of the grain boundary. For a complete understanding of the electronic structure at this disordered grain boundary calculations of the atomistic and the electronic structure are needed which are not available for technical reasons (e.g. computing times, hardware performance) at the present state. The explicit influence of segregated Fe to the grain boundary has not been accounted for in this discussion.

4.3. Delocalization of the EELS interaction in the valence region

The width of the grain boundary region is well known from HRTEM experiments to be approximately 0.6–0.9 nm [22,52]. In STEM experiments the probe size of the primary beam leads to a significant enlargement (factor 2) of the measured grain boundary width if the grain boundary width in the specimen and the probe size are of similar dimensions, as they were in this work.

For spatially resolved valence electron excitations, quantum mechanical effects of delocalization have to be taken into account [8,9,11,18]. Pennycook and Narayan have predicted a delocalization b proportional to $v/\sqrt{(\Delta E^2 \ln(4E/\Delta E))}$ [8], where ΔE is the energy loss, E the primary energy (here 100 keV) and v the velocity of the electrons. Muller and Silcox [9] have measured the inelastic decay length to be proportional to $\Delta E^{-1.0064}$ which provides even stronger effects of delocalization than the model of Pennycook and Narayan [8]. Therefore, grain boundary widths obtained by VEELS measurements are given by a convolution of the real width in the specimen, the size of the probe size used in the experiment and by energy-dependent delocalization effects. In this work we have chosen the width (FWHM) of the dip in the data surface at any particular energy (cf. Fig. 6) for measuring the upper limit of the delocalization of the inelastic scattering process at that energy. The FWHM values of the widths were plotted versus energy-loss in Fig. 12 together with the approximation by Pennycook and

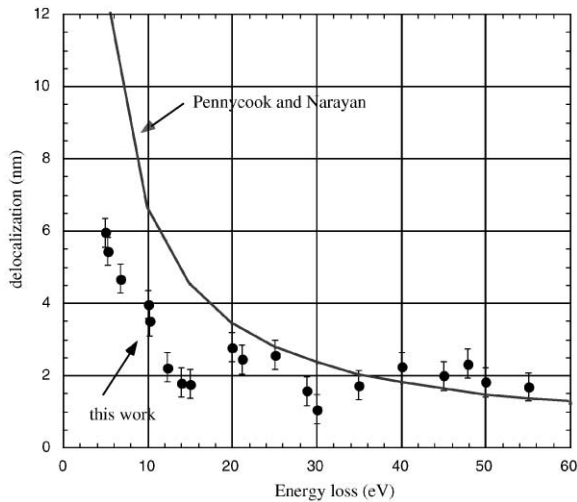


Fig. 12. Delocalization of the inelastic scattering process measured by the FWHM of the width of the $\Sigma 13$ GB obtained by VEELS in comparison to an approximation by Pennycook and Narayan [8].

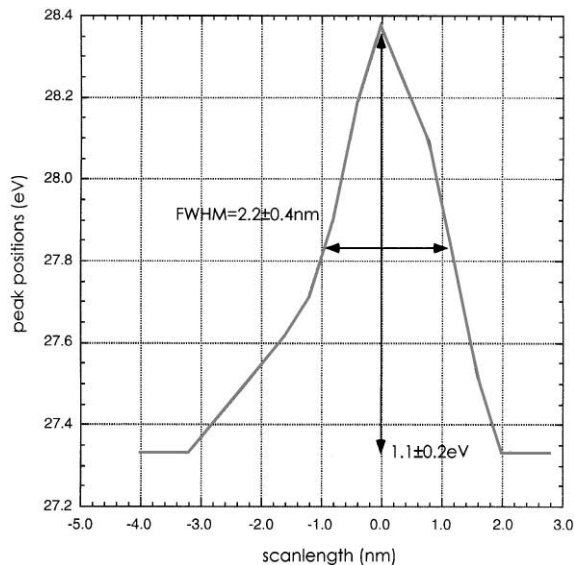


Fig. 13. Measured transition energy for peak F as a function of relative distance. The effective width of the boundary region is determined by the FWHM of the given line shape.

Narayan [8]. One can conclude that these approximations overestimate the delocalization effects in the valence electron region for SrTiO_3 . For energy-losses greater than approximately 15 eV our results

show nearly a constant width of 2.2 nm of the dip in the data surface. In Fig. 13 the energetic peak shift of transition F is plotted versus the scanlength. The full-width at half-maximum (FWHM) of this line shape is 2.2 ± 0.4 nm and provides the nominal width of the grain boundary band structure obtained by VEELS. Therefore, the delocalization effects for the investigated $\Sigma 13$ grain boundary in Fe-doped SrTiO_3 are overestimated by the approximations given by Refs. [8, 9] for energy losses below 15 eV. For higher energy losses delocalization effects become negligible compared to the purely geometric effects, i.e. probe size and grain boundary width in the specimen.

4.4. Dispersion forces at the $\Sigma 13$ boundary

The $\Sigma 13$ grain boundary in SrTiO_3 contains a 0.6–0.9 nm thick disordered intergranular material. This material exhibits iron segregation, a change in the cation ratio, it is well oxidized and has a density as seen from the index of refraction and the f -sum rule which is dramatically lower than in bulk SrTiO_3 . This $\Sigma 13$ boundary can therefore be considered as analogous to an intergranular film between two grains. For this boundary, whose intergranular material has such different physical properties and electronic structure, it is of interest to determine the magnitude of the London dispersion force which is the dominant contributor to the van der Waals forces. The dispersion force at the grain boundary is not expected to be the dominant structural force, since the thermodynamic energies and forces represented by the unsatisfied chemical bonding in the boundary are expected to be dominant. Still the reduced density and changes in chemical bonding of the intergranular material raises the question of the magnitude of the Hamaker constant for the dispersion forces.

From the VUV spectra of single crystal Fe-doped SrTiO_3 the Hamaker constant for SrTiO_3 separated from SrTiO_3 by vacuum ($A_{1|v|}^{\text{NR}}$) is 247 zJ (Table 4). This compares to a value of 195 zJ as determined from the VEELS measurements for the SrTiO_3 grains. The difference in the magnitude of the Hamaker constant between VUV and VEELS

Table 4

Hamaker constants for Fe-doped SrTiO₃ grains (material 1), separated by vacuum or by the intergranular material (material 2) present at the Σ 13 grain boundary

Material 1 spectra	$A_{1 1}^{\text{NR}}$ (zJ) for material 2 of vacuum	$A_{1 2}^{\text{NR}}$ (zJ) for material 2 of Σ 13 intergranular material
VEELS	195 ± 3	83 ± 3
VUV	247 ± 3	120 ± 3

$n(\text{VUV-SrTiO}_3:\text{Fe}) = 2.37$, $n(\text{VEELS-SrTiO}_3:\text{Fe}) = 2.31$,
 $n(\text{VEELS-}\Sigma 13 \text{ intergranular material}) = 1.29$

suggests two different possible causes. One is that the experimental data acquisition and analysis of the VUV and the VEELS data produce results as shown in Fig. 3 which are not quantitatively identical, the second possible cause is that there are differences in the electronic structure of the bulk single crystal sample used in the VUV measurement when compared to the thin foil used in the VEELS measurement. These changes have been discussed in detail in the section of the bulk electronic structure of SrTiO₃.

When the intergranular material of the Σ 13 grain boundary separates the two grains of SrTiO₃, then the Hamaker constant ($A_{1|2}^{\text{NR}}$) is reduced from 195 to 83 zJ, corresponding to a reduction in the London dispersion force by a factor of two due to the presence of this nearly 1 nm thick disordered material. For well-structured, dense, non-disordered interfaces, such as those seen for the Σ 3 and the Σ 5 interfaces [22,52], then the density, the f -sum rule and the index of refraction of the intergranular film would be comparable to the bulk grain, and the Hamaker constant and the London dispersion force at the grain boundary would approach zero. For such well-bonded, dense boundaries, the London dispersion force is expected to be negligible, while for disordered boundaries such as this Σ 13 interface the London dispersion force is larger (83 zJ) than that seen for many ceramic systems such as silica particles in vacuum for which the Hamaker constant is 66 zJ. The magnitude of the Hamaker constant and the London dispersion force at this grain boundary is larger than expected for well-structured, dense, GB.

5. Conclusions

Electronic structure investigations of Fe-doped SrTiO₃ were performed by VEELS and VUV spectroscopy. A comparison of the interband transition strengths obtained by these two experimental methods showed a high level of agreement as far as peak positions and relative peak intensities are concerned. The absolute intensities of the VEELS data are lower than in the VUV data. By comparison to ab initio LDFT calculations assignments for the experimentally observed interband transitions became possible up to transition energies of 22 eV. The results of these investigations are in good agreement with experiments [45] and theoretical investigations [45,49–51] known from literature.

Based on these sets of reference data the electronic structure of a near Σ 13 grain boundary [22,52] was analysed by spatially resolved VEELS measurements. The acquired VEELS linescans show a decrease in intensity in the interband transition strength which is due to a reduced index of refraction and therefore a reduced density of the intergranular film. Kienzle [22,52] found that Fe segregates from the grains to the grain boundary and forms a disordered film of 0.6–0.9 nm width. In this grain boundary region the interband transition strength showed a grain boundary specific line shape and therefore a modified electronic structure compared to the bulk. Decreasing transition strengths for O 2p to metal d transitions in combination with previous energy-dispersive X-ray measurements [22,52] show an enrichment of oxygen vacancies in the disordered grain boundary region. This could also be confirmed by spatially resolved ELNES measurements of the crystal field splitting of the Ti L_{2,3}-edge. Moreover, the Ti atoms are reduced in their nominal oxidation state as indicated by a negative chemical shift.

Calculations of the Hamaker constant and the London dispersion forces showed that their magnitudes in the intergranular film are larger than expected for ordered well-structured GB. Due to the changes in the electronic structure and density of the nanometer thick intergranular material at the Σ 13 interface, the Hamaker

constant and London dispersion force at this boundary is large, and comparable to dispersion forces in other ceramic systems.

For a complete understanding of the electronic structure of the investigated near $\Sigma 13$ grain boundary atomistic and electronic structure calculations are necessary which are not available for such disordered materials at the present state.

By the appearance of grain boundary dependent changes of the VEEL spectra a quantitative analysis of delocalization effects became possible. The FWHM of the dip in the VEELS data was used as a measure for delocalization effects. By comparison to assumptions known from the literature [7,8] a delocalization dependence of smaller than the predicted values was found. Therefore, VEELS analysis represents a reliable method to determine dielectrical properties and electronic structures at high spatial resolution. In addition, by a detailed knowledge of the unoccupied density of states, e.g. by measurements of spatially resolved near-edge structures in electron energy-loss spectra, an indirect determination of the occupied DOS below the Fermi level should become possible with high spatial resolution using VEELS.

Acknowledgements

The authors would like to acknowledge Dr. O. Kienzle for providing the TEM specimens. We thank Lin DeNoyer for the development and her constant improvement of the electronic structure tools. We appreciate discussions with Drs. D. Bonnell and C. Scheu. Thanks are also due to U. Täffner for the specimen preparation for the VUV experiments.

References

- [1] T.K. Gupta, *J. Am. Ceram. Soc.* 73 (1990) 1817.
- [2] V. Ravikumar, R.P. Rodrigues, V.P. Dravid, *J. Phys. D* 29 (1996) 1799.
- [3] N.D. Browning, J.P. Buban, H.O. Moltaji, S.J. Pennycook et al., *Appl. Phys. Lett.* 74 (1999) 2638.
- [4] F. Ernst, O. Kienzle, M. Rühle, *J. Eur. Ceram. Soc.* 19 (1999) 665.
- [5] D.A. Crandles, B. Nicholas, C. Dreher, C.C. Homes et al., *Phys. Rev. B* 59 (1999) 12842.
- [6] M. Leonhardt, J. Jamnik, J. Maier, *Electrochem. Solid State Lett.* 2 (1999) 333.
- [7] R. Waser, *Solid State Ionics* 75 (1995) 89.
- [8] S. Pennycook, Narayan, *Phys. Rev. Lett.* 54 (1985) 1543.
- [9] D.A. Muller, J. Silcox, *Ultramicroscopy* 59 (1995) 195.
- [10] J.M. Titchmarsh, *Ultramicroscopy* 28 (1989) 347.
- [11] R.F. Egerton, *Electron Energy Loss Spectroscopy in the Electron Microscope*, 2nd Edition, Plenum Press, New York, 1996.
- [12] Z.L. Wang, *Micron* 27 (1996) 265.
- [13] A.D. Dorneich, R.H. French, H. Müllejjans, S. Loughin, M. Rühle, *J. Microsc.* 191 (1998) 286.
- [14] R.H. French, H. Müllejjans, D.J. Jones, *J. Am. Ceram. Soc.* 81 (1998) 2549.
- [15] L. Ryen, X. Wang, U. Helmerson, E. Olsson, *J. Appl. Phys.* 85 (1999) 2828.
- [16] L. Normand, A. Thorel, *Electron Microscopy 1998, Proceedings of ICEM-14, Cancun, Mexico, 1998*, p. 625.
- [17] R.H. French, H. Müllejjans, D.J. Jones, G. Duscher, R.M. Cannon, M. Rühle, *Acta Mater.* 46 (1998) 2271.
- [18] R.H. French, *J. Am. Ceram. Soc.* 83 (2000) 2271.
- [19] H. Müllejjans, R.H. French, *J. Phys. D: Appl. Phys.* 29 (1996) 1751.
- [20] H.C. Hamaker, *Physica* 4 (1937) 1058.
- [21] M.L. Bortz, R.H. French, *Appl. Spectrosc.* 43 (1989) 1498.
- [22] O. Kienzle, Ph.D. Thesis, Max-Planck-Institut für Metallforschung, Stuttgart, 1999.
- [23] A. Strecker, U. Salzberger, J. Mayer, *Prakt. Metallogr.* 30 (1993) 482.
- [24] M. Cardona, *Phys. Rev. A* 140 (1996) A651.
- [25] R. Waser, T. Baiatu, K.-H. Härtl, *J. Am. Ceram. Soc.* 73 (1990) 1645.
- [26] R. Waser, T. Baiatu, K.-H. Härtl, *J. Am. Ceram. Soc.* 73 (1990) 1654.
- [27] R. Waser, T. Baiatu, K.-H. Härtl, *J. Am. Ceram. Soc.* 73 (1990) 1663.
- [28] H.A. Kramers, *Atti Congr. Int. Fis. Como.* 2 (1927) 545.
- [29] R. Kroning, *J. Opt. Soc. Am.* 12 (1926) 547.
- [30] R.H. French, D.J. Jones, H. Müllejjans, S. Loughin, A.D. Dorneich, P.F. Carcia, *J. Mater. Res.* 14 (1999) 4337.
- [31] R.H. French, *Phys. Scripta* 41 (1990) 404.
- [32] M.L. Bortz, R.H. French, *Appl. Phys. Lett.* 55 (1989) 1955.
- [33] VEELS.ab v.6.9, Kkeels.ab v.7.5. components of Electronic Structure Tools, Spectrum Square Associates, 755 Snyder Hill Road, Ithaca, NY 14850, USA, which run under GRAMS/32, Galactic Industries, 325 Main Street, Salem NH 03079, USA.
- [34] D.Y. Smith, Dispersion theory, sum rules, and their application to the analysis of optical data, in: E.D. Palik (Ed.), *Handbook of Optical Constants of Solids*, Academic Press, New York, 1985, pp. 35–68.

- [35] K. van Benthem, R.H. French, W. Sigle, C. Elsässer, M. Rühle, to be submitted.
- [36] B. Johs, R.H. French, F.D. Kalk, W.A. McGahan, J.A. Woollam, *Opt. Interference Coat. SPIE* 2253 (1994) 1098.
- [37] P. Hohenberg, W. Kohn, *Phys. Rev.* 136 (1964) B864.
- [38] W. Kohn, L.J. Sham, *Phys. Rev.* 140 (1965) A1133.
- [39] D.M. Ceperly, B.J. Alder, *Phys. Rev. Lett.* 45 (1980) 566.
- [40] J.P. Perdew, A. Zunger, *Phys. Rev. B* 23 (1981) 5048.
- [41] S.G. Louie, K.M. Ho, M.L. Cohen, *Phys. Rev. B* 19 (1979) 1974.
- [42] C.L. Fu, K.M. Ho, *Phys. Rev. B* 28 (1983) 5480.
- [43] C. Elsässer et al., *J. Phys.: Condens. Matter* 2 (1990) 4371.
- [44] B. Meyer, Ph.D. Thesis, Universität Stuttgart, 1998.
- [45] D. Bäuerle, W. Braun, V. Saile, G. Sprüssel et al., *Z. Phys. B* 29 (1978) 179.
- [46] V.E. Henrich, G. Dresselhaus, H.J. Zeiger, *Phys. Rev. B* 17 (1978) 4908.
- [47] L.F. Mattheiss, *Phys. Rev. B* 6 (1972) 4718.
- [48] S.G. Louie, J.R. Chelikowsky, M.L. Cohen, *Phys. Rev. Lett.* 34 (1975) 155.
- [49] Y.-N. Xu, W.Y. Ching, R.H. French, *Ferroelectrics* 111 (1990) 23.
- [50] Shang-Di Mo, W.Y. Ching, M.F. Chisholm, G. Duscher, *Phys. Rev. B* 60 (1999) 2416.
- [51] F.M.F. de Groot, J. Faber, J.J.M. Michiels, M.T. Czyzyk, M. Abbate, J.C. Fuggle, *Phys. Rev. B* 48 (1993) 2074.
- [52] O. Kienzle, M. Rühle, in: *Proceedings of EUROMAT'99*, Wiley VCH, 2000.
- [53] N.D. Browning, S.J. Pennycook, *J. Phys. D: Appl. Phys.* 29 (1996) 1779.
- [54] J. Bruley, *Microsc. Microanal. Microstruct.* 4 (1993) 23.
- [55] R.D. Leapman, L.A. Grunes, P.L. Fejes, *Phys. Rev. B* 26 (1982) 614.